J Nanopart Res (2012) 14:1107
DOI 10.1007/s11051-012-1107-y

RESEARCH PAPER

Tuning the dipole-directed assembly of core-shell nickel-coated gold nanorods

Chris Hellenthal · Waqqar Ahmed · E. Stefan Kooij · Arend van Silfhout · Bene Poelsema · Harold J. W. Zandvliet

Received: 7 May 2012 / Accepted: 27 July 2012 / Published online: 11 August 2012

Abstract We present the dipole-directed assembly of nickel-coated gold nanorods into nanorings and nanowires. We used two different coating methods to synthesise these core-shell superstructures. Surprisingly, the two coating methods lead to very different kinds of dipole directed assembly. We show that the resultant dipole assembly is very sensitive to the reaction conditions and can be tuned to obtain core-shell nanochains, nanorings, and nanowires. In addition to the presented experimental work, cluster moving Monte Carlo simulations of a system of core-shell nanorods were carried out. These simulations are based on a small number of magnetic interaction energy terms and do not explicitly deal with steric interactions or van der Waals forces. The simulation results are in line with the obtained experimental results, confirming that the magnetic self-assembly of core-shell nanorods can be described by means of a relatively simple model.

C. Hellenthal · E. S. Kooij (✉) · A. van Silfhout · B. Poelsema · H. J. W. Zandvliet
Physics of Interfaces and Nanomaterials, MESA+ Institute for Nanotechnology, Faculty of Science and Technology, University of Twente, PO Box 217, 7500 AE Enschede, The Netherlands
e-mail: e.s.kooij@utwente.nl

W. Ahmed
Department of Physics, COMSATS Institute of Information Technology, Park Road, Islamabad, Pakistan

Keywords Core-shell · Nanorod · Self-assembly · Monte Carlo · Gold · Nickel

Introduction

The manufacture of nanostructures has attracted enormous attention recently due to the unusual properties of these structures and their potential applications in nano-electronics, sensors, magnetic data storage devices, and many other areas (Sun et al. 2003; Shevchenko et al. 2003; Zitoun et al. 2002; Sobal et al. 2002; Schmid 2004; Hyeon 2003; Pacholski et al. 2002). Self-assembly is a simple and elegant technique to synthesize novel nanostructures with interesting new properties. For the synthesis of magnetic nanostructures, magnetic dipole-directed self-assembly can be exploited. This technique has been used in several recent studies into the self-assembly of chains (Wang et al. 2008, 2009; Liu et al. 2004), rings, (Xiong et al. 2007; Ahmed et al. 2010) and bracelets (Tripp et al. 2002; Wei et al. 2009) of magnetic nanoparticles.

One way of tuning dipole-directed assembly is to coat a non-magnetic core nanoparticle with a magnetic shell. By controlling the thickness of the magnetic shell, the dipolar interaction strength, and therewith the assembly, can be controlled. We have recently shown preliminary results which demonstrate that the nickel coating of rod-shaped gold nanoparticles results in

their self-assembly into nanorings in solution (Ahmed et al. 2010). The assembly of these particles can be tuned by controlling the concentration of nickel present in the growth solution. Before the coating of gold nanorods with nickel, they should first be functionalised with platinum, which acts as a catalyst for the nickel reduction on gold nanorods (Grzelczak et al. 2007). More recently, Sajanlal and Pradeep (2010) have reported that the nickel coating of gold nanoparticles can be achieved without the need for the catalytic effect of platinum if the reaction is carried out at higher pH values. The reaction in this case is very fast and completes within 2 min, in contrast to the platinum-assisted method where at least 3 h are needed for the complete reduction of nickel onto gold nanorods. The availability of two different procedures with very different reaction conditions inspired us to study their effect on dipole-directed assembly. In addition, we decided to simulate the dipole-directed assembly to gain insight into the way in which the assembly varies with the thickness of the nickel coating.

Computer simulations of magnetic nanoparticles have been performed in the past. Various magnetic interactions have been studied, including those between spherical (Morimoto et al. 2009; Wen et al. 1999; Tavares et al. 2002) or cubic (Zhang et al. 2007) nanoparticles, as well as the atomic-scale interactions within nanoparticles (Kodama and Berkowitz 1999). Recently, Aoshima and Satoh (2006) have reported results obtained from simulations of rod-like particles using a magnetic charge model, as well as a model incorporating a single magnetic dipole (Satoh 2008). Such simulations provide a valuable tool in predicting and understanding the interactions between magnetic nanoparticles.

In this study, we present the results of a study to analyse the effect of the two coating methods on the dipole-directed assembly of nickel-coated gold nanorods. To our surprise, the results of the assembly were remarkably different for the two methods. The difference in assembly arises from the different reaction conditions in these two cases. The performed Monte Carlo simulations clearly show the influence of various system parameters on the final assembly. Using the right input parameters, the simulation results can be made to resemble the results of physical experimentation, showing that ring formation can be modelled by means of only magnetic interactions.

Experimental

Chemicals

Cetyl trimethylammonium bromide (CTAB), $NaBH_4$ (both ≥99 % purity), K_2PtCl_4 (≥99.99 % purity), and $HAuCl_4$ (≥99.999 % purity) were purchased from Sigma-Aldrich. $AgNO_3$ (≥99.85 % purity), $NiCl_2$ (≥99.999 % purity), and hydrazine hydrate (100, and 64 % hydrazine) were purchased from Acros Organics. HCl, NaOH, and ascorbic acid (all analytical grade) were purchased from Merck. All solutions were prepared using ultra-pure water (millipore; 18.2 MΩ cm).

Gold nanorod synthesis

Gold nanorods were prepared by a previously described seeded growth protocol with some modifications (Nikoobakht and El-Sayed 2003; Liu and Guyot-Sionnest 2005). For the preparation of seeds, chloroauric acid was used. To 10 mL of 0.1 M CTAB, 25 μL of gold stock solution (0.1 M $HAuCl_4$) was added. While stirring, 60 μL of 0.1 M ice cold $NaBH_4$ was added, and stirring continued for 2 min. The solution turned light-brown right after the addition of $NaBH_4$, indicating particle formation. For the growth solution, 10 mL of 0.1 M CTAB was mixed with 50 μL gold stock solution. After this, 100 μL of 0.01 M $AgNO_3$ was added, followed by the addition of 70 μL of 0.1 M ascorbic acid, and the growth solution quickly turned from dark yellow to clear and colourless. To this solution, 50 μL of 0.1 M HCl solution was added to decrease the pH of the solution to 2–3. Subsequently, 24 μL of CTAB-capped seeds was added and the resulting solution was left overnight at 25 °C. The resultant solution was centrifuged once at 5,200 rpm for 6 min. During centrifugation, the unwanted large spherical nanoparticles sink to the bottom of the centrifuge tube, leaving a supernatant with a higher relative concentration of nanorods. This supernatant was collected, after which the procedure was repeated one additional time to further reduce the amount of spherical particles in the solution. The estimated concentration of nanorods after centrifugation is 7.5×10^{14} m^{-3}. Sample preparation was performed by centrifuging the particle solution at 10,000 rpm for 10 min and redispersing the precipitates in equal volume clean water (Millipore; 18.2 MΩ

cm). This procedure was repeated one additional time, after which a 5 μL drop of solution was deposited on a clean Si/SiO_2 substrate and allowed to dry under ambient conditions.

Platinum-assisted coating method

By means of this method, gold nanorods were first functionalised with platinum. For platinum coating of gold nanorods, we started with 10 mL of nanorod suspension, added to 20 mL of 0.1 M CTAB, followed by addition of 110 μL of 0.04 M K_2PtCl_4 solution. The solution was left for half an hour at 40 °C for complexation of platinum with CTAB. For the reduction of platinum, 940 μL of 0.1 M ascorbic acid was added and the solution was left at 40 °C overnight. The next day, the solution was centrifuged twice at 10,000 rpm for 10 min, and the precipitates were re-dispersed in equal volumes of 0.1 M CTAB solution. The platinum-coated nanorods were further coated with nickel, using hydrazine as a reducing agent. Four different solutions were prepared. For all solutions, 2.5 mL of platinum-coated nanorod solution was added to 22.7 mL of clean water (Millipore; 18.2 MΩ cm), followed by the addition of 21, 36, 50, and 67 μL of 0.25 M $NiCl_2$. This was followed by addition of 75, 125, 175, and 240 μL of 5.72 M hydrazine solution, respectively. It should be noted that the final concentration of the surfactant CTAB in solution is 0.01 M. The solutions were kept at 40 °C for 3 h. Afterward, the nickel-coated nanorods were separated by a handheld magnet and washed twice with clean water before redispersion in equal volume clean water. The estimated concentration of nanorods after centrifugation is 2.5×10^{13} m^{-3}. The successful coating with nickel was confirmed by the ultraviolet-visible (UV-Vis) spectroscopy of solutions. The characteristic absorption peaks of gold nanorods had vanished, showing the successful coating of gold nanorods with nickel. Five microlitres of each solution was dried under ambient conditions on a separate Si/SiO_2 substrate for microscopy analysis.

Fast coating method

This coating procedure was adapted from the method reported by Sajanlal and Pradeep (2010). The previously prepared gold nanorod solution was centrifuged twice and the precipitates were re-dispersed in water. Four different solutions were prepared. For all solutions, 500 μL of 0.1 M NaOH was added to 5 mL of nanorod solution, raising the pH of the solution to approximately 11. This was followed by the addition of 7, 14, 21, and 28 μl of 0.25 M of $NiCl_2$. After that, 220, 445, 670, and 890 μL of hydrazine was added, respectively. The reaction was carried out at 80 °C. The colour of the solution changes from brown to blackish in 5 min. The coated nanorods were extracted from the solution using a handheld magnet and washed with clean water. Afterward, the particles were redispersed in equal volume clean water. The estimated concentration of nanorods after centrifugation is 6.3×10^{14} m^{-3}. Five microlitres of each solution was dried under ambient conditions on a separate Si/SiO_2 substrate for microscopy analysis.

Characterisation

UV-Vis absorption measurements were carried out using an Ocean Optics HR2000+ high-resolution spectrometer, combined with a Mikropack DH-2000-BAL lightsource.

Helium ion microscopy (HIM) images were obtained using a Carl Zeiss SMT Orion Plus system.

The scanning electron microscopy (SEM) images presented in this study were obtained using a Zeiss 1550 HR-SEM LEO system.

Transmission electron microscopy (TEM) measurements were performed using a Phillips CM 300ST system.

Results and discussion

Gold nanorod characterisation

Figure 1a shows an image of the as-prepared gold nanorods. As evident from the image, there is a significant concentration of spherical particles. UV-Vis spectrum (Fig. 1c, solid line) contains a strong absorption peak at 550 nm, which is indicative of the presence of these spherical particles. The transverse absorption peak of the gold nanorods would normally appear at approximately 500 nm for gold nanorods of aspect ratio 4–5 (Kooij and Poelsema 2006). Therefore, we can conclude that the peak around 550 nm is a consequence of the presence of relatively large

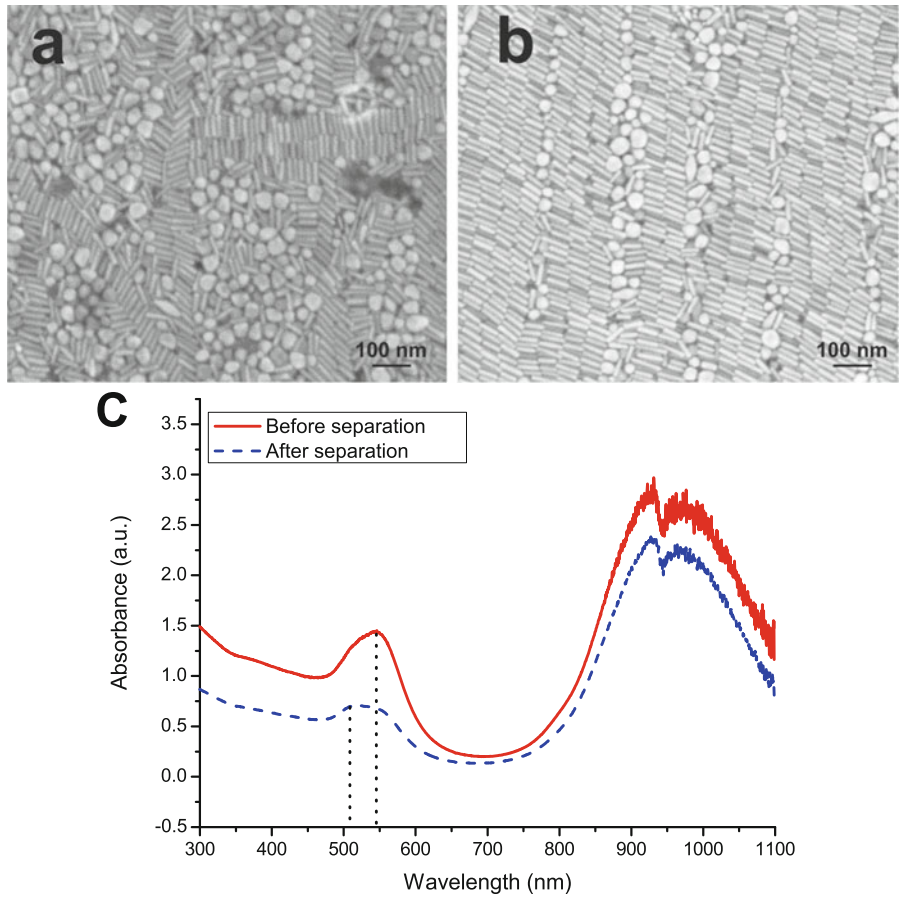

Fig. 1 SEM images of gold nanorods **a** before separation, **b** after separation and **c** UV-Vis spectra of both suspensions. The "dip" around 950 nm was caused by an instrumentation error; spectra have not been normalised. (colour online)

spherical particles. About 30 % of the particles are spherical, as determined from several images.

We found that if the nanorod suspension is centrifuged at 5,200 rpm for 6 min, the spherical particles sink to the bottom due to their higher mass and the remaining supernatant will have a higher relative concentration of nanorods. By employing centrifugation, we were able to reduce the concentration of spherical particles in the solution from 30 % to about 4 %. Figure 1b shows an image of the particles that were obtained after this centrifugation step. As evident from the image, the relative concentration of nanorods in this case is much higher than before centrifugation (Fig. 1a). This difference is also evident from the UV-Vis absorption spectrum (Fig. 1c, dashed line). The overall loss of intensity at smaller wavelengths is caused by the lower concentration of particles. On top of that, the relative intensity of the plasmon peak around 550 nm is decreased and the peak is blue-shifted to 505 nm. There is only a slight decrease in the intensity of the longitudinal plasmon peak at 950 nm, which means that a small amount of nanorods was lost during the process of centrifugation. The remaining nanorods have an average length of 53.7 ± 6.1 nm and an average width of 12.1 ± 1.5 nm, which gives them an aspect ratio of 4.5 ± 0.8. This aspect ratio matches the longitudinal absorption peak around 950 nm. We have found no indication that the presence of the remaining spherical particles had a significant effect on the experiments described in this study.

Nickel coating of gold nanorods

The results of the platinum-assisted coating method can be seen in Fig. 2. The nickel-to-gold ratios of the used growth solution, as well as the estimated nickel shell thickness, are mentioned in the caption. The nickel shell thickness was determined by measuring the diameter of individual rods and subtracting the gold core diameter. Figure 2a depicts the nickel-coated gold nanorods that have been synthesised using

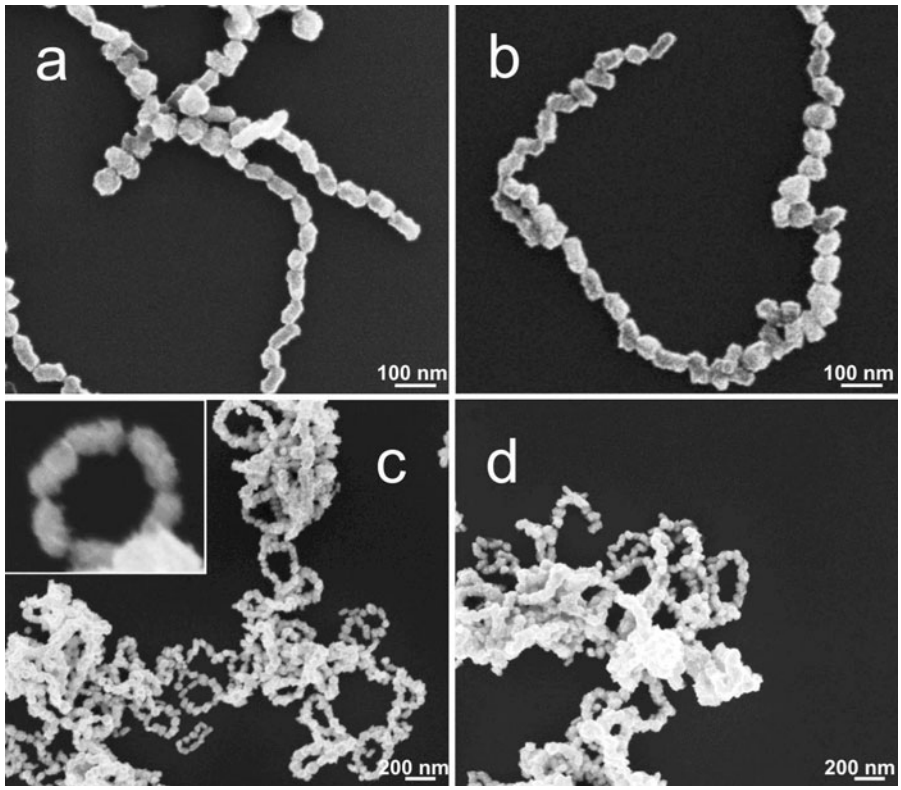

Fig. 2 HIM (**a**, **b**) and SEM (**c**, **d**) images of dipole-directed assembly of nickel-coated gold nanorods. The amount of nickel added to the growth solution, the corresponding Ni:Au ratios and the estimated shell thicknesses were 21 μL (55:1, 13.4 nm) (**a**), 36 μL (95:1, 15.2 nm) (**b**), 50 μL (130:1, 17.8 nm) (*inset* shows magnified image of a single ring) (**c**) and 67 μL (175:1, 19.3 nm) (**d**)

the lowest concentration of nickel. The aspect ratio of the nanorods has visibly decreased due to the nickel coating, which suggests that the coating is isotropic over the entire surface of the nanorods. This isotropic overcoat was also observed for aspect ratio 3 nanorods in previous experiments (Ahmed et al. 2010). Furthermore, as evident from the image, the rods assemble in a head-to-tail fashion, probably as a result of dipolar interactions. Considering that the particles assemble along their dipole axis under the influence of magnetic dipolar interactions, the head-to-tail assembly implies that the long axis of the nanorods is the easy axis of magnetisation. This was to be expected due to the shape anisotropy of the particles. Increasing the concentration of nickel present in the growth solution increases the thickness of the nickel coating on the nanorods, as evident from Fig. 2b, but still only chain formation is observed. However, comparing several microscopy images shows that increasing the nickel coating thickness increases the probability of particle chains closing into circular rings. For even higher concentrations of nickel, the particles assemble into rings as can been seen in Fig. 2c, d. Aside from a few exceptions, these rings appear to be solid structures consisting of nickel-coated gold nanorods with an additional overcoating of nickel, similar to the rings that were observed during the coating of aspect ratio 3 nanorods (Ahmed et al. 2010). The presence of these solid rings indicates that rings form during synthesis in the presence of unreacted nickel, which is subsequently reduced onto the formed nanorings. As such, we can conclude that the formation of individual rings is not due to any type of drying effect or capillary interaction. The fact that the nanorod solutions are rather dilute (see "Platinum-assisted coating method" section) further supports this claim. Figure 3 shows the EDX and TEM characterization of a nickel-coated gold nanorod prepared using the platinum-assisted coating method. These results confirm that the growth of the nickel coating on the gold nanorods is quasi-epitaxial, as was reported before by Grzelczak et al. (2007).

Figure 4 depicts the images of nickel-coated gold nanorods prepared by the fast coating method with different concentrations of nickel. Figure 4a shows an image of nickel-coated nanorods prepared with a Ni:Au ratio of 10:1. The coated nanorods tend to assemble in a one-dimensional chain. Occasionally,

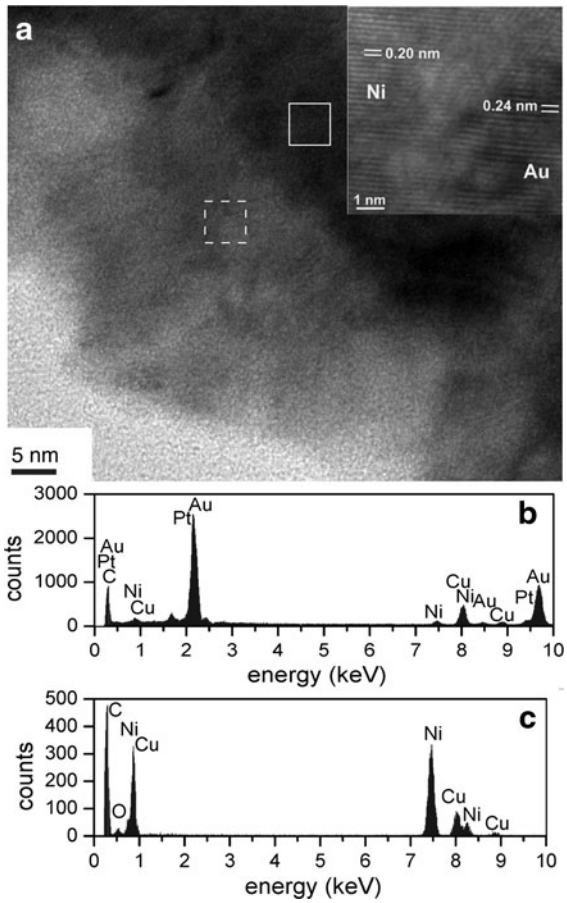

Fig. 3 Characterisation of a gold nanorod coated by the platinum-assisted coating method. **a** TEM image of nickel-coated gold nanorod. The *inset* shows a lattice-resolved TEM image of the interface between the rod and the coating, demonstrating the quasi-epitaxial growth. **b** EDX spectrum of the coated rod as indicated by the *solid square*. **c** EDX spectrum of the nickel coating as indicated by the *dashed square*

the coated nanorods are connected to one another by an overcoat of nickel. Raising the Ni:Au ratio to 20:1 resulted in an improved nanorod assembly into nanowires as can be concluded from Fig. 4b. It should be noted, however, that the particles do not assemble in a head-to-tail fashion as they do for the platinum-assisted coating method; the assembly takes on a branched shape. Further increasing the nickel concentration results in an overcoat of the already formed one-dimensional structures by nickel, as evident from Fig. 4c. A Ni:Au ratio of 40:1 results in a thicker overcoat of nickel, leading to nanowire formation as shown in Fig. 4d. As is the case for ring formation, the overcoat of the formed structures strongly suggests that they are formed in solution. As discussed by Sajanlal and Pradeep (2010), the nickel layer deposited through the use of this fast coating method is polycrystalline. Note that no external magnetic field was present during synthesis or sample preparation.

The results obtained by the fast coating method are remarkably different from those obtained by the platinum-assisted coating method. After calculating the nickel-to-gold ratios used in both methods, we found that much smaller nickel-to-gold ratios lead to thicker coatings when using the fast coating method. Comparing the coated particles in Figs. 2a and 4d, which were prepared with similar nickel-to-gold ratios, clearly shows that the coating is much thicker in the latter case. The unsaturated reduction of nickel in the platinum-assisted method could be the cause of this difference. It is known that during seeded growth of gold nanorods, only 15 % of the initial gold ions in the growth solution are completely reduced (Orendorff and Murphy 2006). The same may hold for the nickel reduction during the platinum-assisted coating method. The reduction of nickel for the direct coating method seems to be more efficient, likely due to the higher hydrazine concentrations and elevated temperatures at which the process takes place. This also explains why the increase of nickel shell thickness is more "linear" for the fast coating method than it is for the platinum-assisted coating method.

It is interesting to note that when using the fast coating method, only one-dimensional chain assembly is seen, in contrast to the platinum-assisted method where ring formation was observed. The assembly in the platinum-assisted method, however, also starts with chain formation. As evident from Fig. 2a, b, the coated nanorods first assemble in chains, which subsequently close into rings for higher nickel concentrations (Fig. 2c, d). The difference in the two coating methods, in addition to the presence of a catalyst, is the coating time. For the platinum-assisted method, the nickel coating is slow and takes 3 h to complete. This gives particles enough time to minimise their energy by assembling head-to-tail into chains, which then bend or merge into rings. We suggest that in the fast coating method, the reaction is too fast for the particles to settle themselves into a minimum energy state (i.e., flux closure rings), leading to a less well-ordered head-to-tail assembly. Furthermore, coating occurs too fast for the chains to join their ends to form rings.

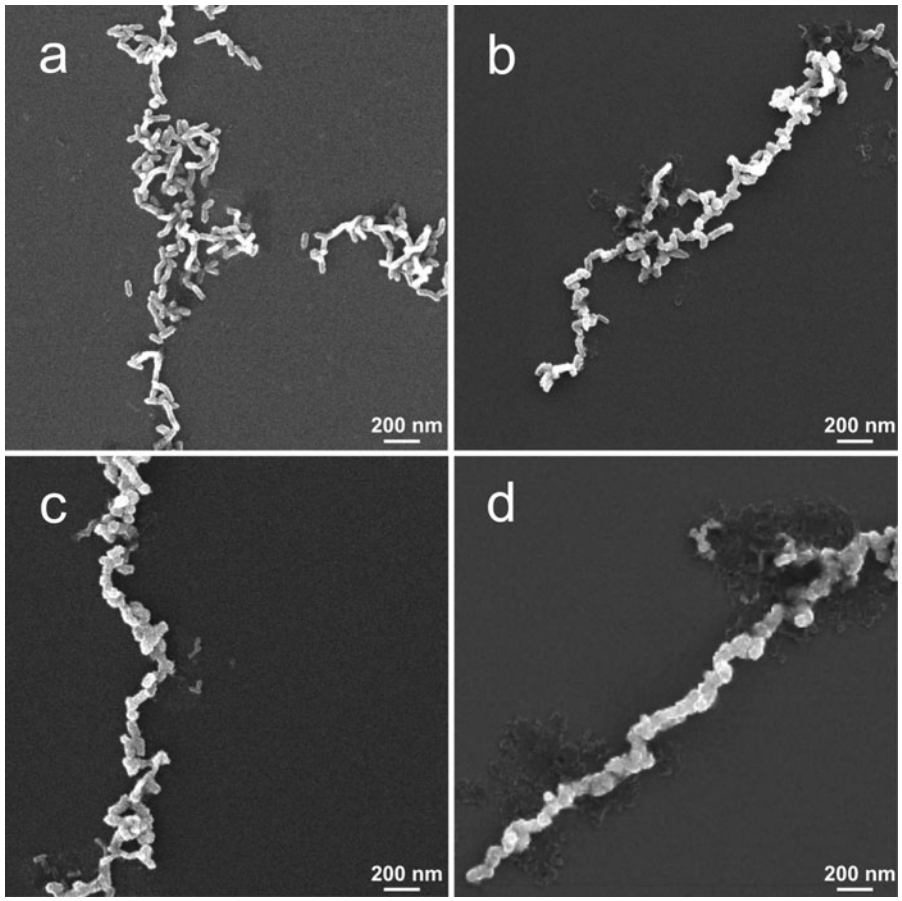

Fig. 4 HIM images of nickel-coated gold nanorods that have been prepared by the fast coating method. The amounts of nickel added to the growth solution, the corresponding Ni:Au ratios and the estimated shell thicknesses were 7 μL (10:1, 8.6 nm) (**a**), 14 μL (20:1, 13.7 nm) (**b**), 21 μL (30:1, 23.1 nm) (**c**), and 28 μL (40:1, 31.2 nm) (**d**)

Another difference between the two coating methods is the absence of a surfactant during the fast coating method. In the platinum-assisted coating method, 10 mM of the surfactant CTAB is present in solution during the coating. It has been postulated that, similar to gold nanoparticles, nickel nanoparticles, when grown in the presence of CTAB, are stabilised by the bilayer of CTAB (Johnson et al. 2002; Gao et al. 2003; Wu and Chen 2004; Chen and Hsieh 2002). The existence of a bilayer of CTAB on the surface of the particles will stabilise them against agglomeration due to van der Waals forces. This, in turn, results in the dominance of anisotropic dipolar interactions during the assembly process (Butter et al. 2003). For the rod-shaped nanoparticles, it is energetically favourable for the magnetic moment to point along the long axis (Vereda et al. 2009). Therefore, after the neutralisation of van der Waals forces by steric repulsions, the nanorods assemble in a head-to-tail fashion under the influence of magnetic dipolar forces. But, in case if there is no surfactant present during the assembly process, van der Waals forces can be very effective at short distances and could contribute to the assembly process. During the fast coating method, nanorods are first attracted by magnetic dipolar interactions. Once the nanorods have been brought into close proximity by the magnetic interactions, the van der Waals forces begin influencing them. Ultimately, the combined effect of magnetic and van der Waals interactions results in a branched assembly. The absence of any surfactant, and therewith, the absence of steric repulsions causes the van der Waals

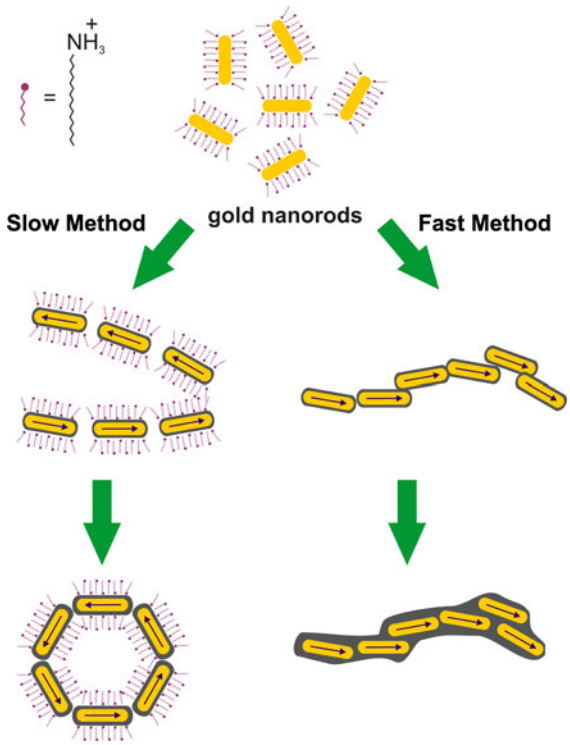

Fig. 5 Schematic of the dipole directed assembly process for the platinum-assisted method (*left*) and fast coating method (*right*) (colour online)

forces to play a considerable role in directing the assembly of particles side-by-side in order to maximise the contact between the particles (cf. Fig. 1a, b).

The mechanism proposed for ring formation is schematically illustrated on the left side of Fig. 5. When the non-magnetic gold nanorods are coated with nickel they acquire a magnetic moment, which causes them to interact with each other. For a sufficiently thick coating layer, the particles overcome the Brownian motions and assemble into chains. When using the platinum-assisted coating method, particles have enough time to assemble properly in a head-to-tail configuration, which is energetically favourable. Further growth of the nickel layer on the gold nanorods leads to closing of the chain ends for the platinum-assisted coating method, resulting in nanoring formation.

The formation of nanorings is also assisted by the presence of a surfactant. However, for the fast coating method, the fast rate of reaction, combined with the absence of a surfactant, leads to a branched assembly. Additional coating of this branched assembly results in the formation of core-shell nanowires as shown schematically on the right side of Fig. 5.

Computational model

In order to provide a theoretical basis for our experimental results, we carried out magnetic field simulations by means of a cluster moving Monte Carlo algorithm (Satoh 1992). It must be noted that the algorithm used in these simulations gives the final state of the particles by minimising their free energy. As such, it is only applicable to nanorods which have been coated by the platinum-assisted coating method, as these have enough time to reach their minimum free energy state during their assembly.

The model particles have a hemispherically capped cylinder geometry and are defined as a core-shell system consisting of a non-magnetic core and an isotropic magnetic shell as shown schematically in Fig. 6. After initialisation, each particle has a position vector indicating the position of the centre of the particle $\mathbf{r}(r_x, r_y, r_z)$, an orientation vector $\mathbf{v}(v_x, v_y, v_z)$, and a magnetisation vector $\mathbf{M}(M_x, M_y, M_z)$. The physical particle boundaries are also defined via $\mathbf{v}$ with the particle long axis aligned parallel to it. The particle has a short diameter of d_t and a long diameter of L_t with the aspect ratio defined as $\chi = \frac{L_t}{d_t}$ (for $\chi = 1$ the particle is spherical). In addition to the dimension of the entire particle, the dimensions of the non-magnetic core are also defined through the parameters d_c and L_c. It should be noted that the particles are confined to the x,y-plane, i.e., $r_z = v_z = 0$. In addition, the particles are confined to a limited area via an infinite potential well. The simulation starts with distributing N particles uniformly over this area, which has a size given by

$$A = \frac{{d_t}^2 N \chi}{\xi}, \tag{1}$$

where $0 < \xi < 1$ indicates the fraction of the area covered with nanoparticles.

For the calculation of the dipole–dipole interaction, the particle is divided into a number of point dipoles. These point dipoles have an interaction with all other point dipoles, excluding those that are part of the same particle. The accuracy of the calculation of the dipole–dipole interaction energy between the particles

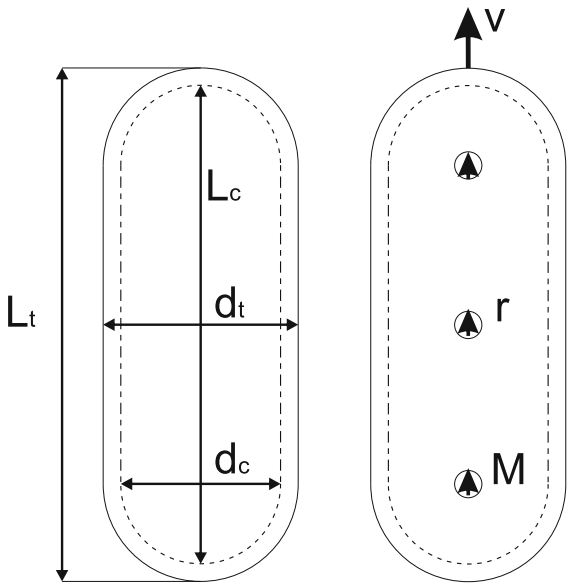

Fig. 6 Schematic representation of the particle geometry. The *dashed lines* indicate the non-magnetic core particle

increases with the number of dipoles per particle. However, the calculation time rises quadratically with the number of dipoles, making it unfeasible to use a large number of dipoles. As such, the choice was made to use three dipoles per particle. Two of these dipoles are situated at the ends of the cylindrical part of the particles, while the third one is positioned in the centre of mass of the particle, as can be seen in Fig. 6. The magnetic field of a spherical shell can be approximated by that of a single dipole placed at the centre of that shell (Griffiths 1999). As such, the chosen positions of the three dipoles should give a good approximation of the magnetic coating. The chosen dipole distribution strikes a balance between computation time and accuracy, and insures that the end-caps, as well as the centre of the particle, have sufficient magnetic interaction with the rest of the system. Using the three dipole configuration does not introduce a "bias" for a certain alignment as was observed for a one dipole configuration (biased toward anti-parallel ordering) or a two dipole configuration (biased toward head-to-tail ordering). Note that for a spherical particle, all dipoles will be situated in the centre of mass. The strength of each of the three dipoles is equal to one third of the total magnetic dipole moment of the entire particle. All three dipoles of a single particle point in the same direction indicated by **M**.

Every particle in the system has a potential energy dependent on the positions, orientations, and magnetisations of all particles in the system. The most significant contribution to the energy of the system comes from the dipole–dipole interaction which, for two arbitrary dipoles, is given by

$$E_{\mathrm{dip}} = \frac{\mu_0}{4\pi}\left[\frac{\mathbf{m_i}\cdot\mathbf{m_j}}{r_{\mathrm{ij}}^3} - \frac{3}{r_{\mathrm{ij}}^5}(\mathbf{m_i}\cdot\mathbf{r_{ij}})(\mathbf{m_j}\cdot\mathbf{r_{ij}})\right], \tag{2}$$

where $\mathbf{m_i}$ is the magnetic dipole moment of dipole i and $\mathbf{r_{ij}}$ is the separation vector between dipole i and j with the magnitude r_{ij}. To obtain the dipole–dipole interaction energy of a single particle, the sum of the interactions of that particle's dipoles with all other dipoles in the system should be determined.

Another important magnetic energy to consider is the magnetostatic self-energy of the particles, given by (Vereda et al. 2009)

$$E_{\mathrm{D}} = \frac{1}{2}\mu_0 V \mathbf{M}\cdot\mathbf{N_D}\cdot\mathbf{M}. \tag{3}$$

where **M** is the magnetisation vector of the particle and V is the effective magnetic volume of the particle (see Eq. 6). $\mathbf{N_D}$ is the demagnetisation tensor in the particle reference frame, given by (Vereda et al. 2009)

$$\mathbf{N_D} = \begin{bmatrix} 1-C & 0 & 0 \\ 0 & C/2 & 0 \\ 0 & 0 & C/2 \end{bmatrix}, \tag{4}$$

where C is the geometry factor for a spheroid given by (Shine and Armstrong 1987)

$$C = \frac{(a/b)^2}{(a/b)^2 - 1} - \frac{(a/b)\cosh^{-1}(a/b)}{[(a/b)^2 - 1]^{\frac{3}{2}}}, \tag{5}$$

where a and b are the long and short diameter of the particles, respectively. Note that Eq. 4 requires the long axis of the particle to point along the x-axis in the frame of reference. Considering the actual shape of the nanoparticles (hemispherically capped cylinder), Eqs. 4 and 5 only approximate the actual demagnetisation tensor of the particles. The demagnetisation tensor for the hemispherically capped cylinder geometry could be determined through the use of micromagnetic simulations, but this falls outside the scope of the current work. Owing to their size, the nanoparticles can be treated as being single domain (i.e., magnetised to saturation), with the saturation magnetisation equal to 483 kA m^{-1} (Vereda et al. 2009).

The strength of the magnetic interactions is directly related to the magnetic dipole moment of the particle, which in turn is dependent on the volume of magnetic material in the particle. The volume used when calculating the magnetic interactions is equal to the volume of the magnetic shell of the particle and is given by

$$V = \frac{4\pi}{3}\left[\left(\frac{d_t}{2}\right)^3 - \left(\frac{d_c}{2}\right)^3\right] + (L_t - d_t)\pi\left[\left(\frac{d_t}{2}\right)^2 - \left(\frac{d_c}{2}\right)^2\right], \quad (6)$$

as can be seen in Fig. 6.

The thermal energy of the system (i.e., the temperature of the system) is taken into account by inclusion of the Boltzmann factor in the Monte Carlo procedure.

Neither the steric interactions caused by the presence of CTAB nor the van der Waals forces were explicitly treated in the simulation. We have assumed that the repulsive steric interactions effectively nullify the attractive van der Waals forces between particles, making the interactions due to the magnetic coating of the particles the dominant factor in their self-assembly.

To prevent the particles from overlapping, a hard sphere potential was introduced. This term has a value of either 0 (no overlap) or ∞ (overlap with one or more other particles).

Analogous to Satoh (2008), we can define a dimensionless constant λ as an indication of the strength of the magnetic interactions in the system:

$$\lambda = \frac{\mu_0 (MV)^2}{k_b T 4\pi L_t^3} \quad (7)$$

where V is the volume of the magnetic material. The system is made to converge into a minimum free energy configuration by randomly perturbing the orientation and position of the particles. During the course of the simulation, the geometry of the particles stays constant. However, the effective volume used in the calculation of the magnetic interaction energy is increased during the simulation to account for the gradual increase in magnetic material during the coating procedure. Note that the formation of nano-sized superstructures in a (drying) solution is a complex process that depends on a large number of interactions, some of which are not yet fully understood (Min et al. 2008). As such, a completely rigorous treatment of all the interactions involved in assembly formation falls well outside the scope of the present work.

Monte Carlo procedure

The program uses a Monte Carlo procedure similar to the one used by Satoh (1992) to evolve the system into its lowest free energy state. This method is based solely on finding the system state with the lowest free energy via random perturbations; no forces or torques are taken into account. During a single iteration, the following steps are performed for each particle:

1. The particle orientation **v** and magnetisation vector **M** are independently perturbed by a small amount. This is known as a rotational trial move. Every ninth iteration, the particle position **r** is perturbed instead. This is known as a translational trial move. Performing multiple rotational trial moves per translational trial move insures that the particles are aligned properly before they are displaced, preventing them to become "trapped" in a disadvantageous energy state.
2. The total particle energy is calculated. The change in particle energy is calculated by subtracting the old particle energy from the new particle energy: $dE = E(j, i) - E(j, i - 1)$, where j indicates the particle and i indicates the iteration number.
3. If $dE < 0$ the trial move is accepted and the new particle position, orientation, magnetisation, and energy are carried over to the next iteration.
4. If $dE \geq 0$, a random number $0 \leq R \leq 1$ is taken from a uniform distribution.
   (a) If $\exp\left(-\frac{dE}{k_b T}\right) \geq R$, the trial move is accepted and the new particle position, orientation, magnetisation, and energy are carried over to the next iteration.
   (b) If $\exp\left(-\frac{dE}{k_b T}\right) < R$, the trial move is rejected and the particle position, orientation, magnetisation, and energy are reverted to the old state and carried over to the next iteration.

During the course of the simulation, particles will form clusters due to the magnetic interactions between them. Particles will generally not detach from these clusters, causing them to be immobilised. To prevent

the system from stagnating due to cluster formation, the clusters themselves are also moved every iteration. The procedure is similar to the one used for single particles. By repeating this process a large number of times, the system will eventually converge into a situation with the lowest possible free energy.

To simulate the gradual increase of magnetic material during the coating procedure, the simulation starts with an effective magnetic interaction strength of 0.1 (10 %) of its final value. After the simulation has reached a minimum free energy configuration, this value is increased by 0.1. This procedure is repeated until the effective magnetic interaction strength has reached 1 (100 %).

Model results

Nanoparticles with a core aspect ratio of 4.5 were used for all simulations. The thickness of the isotropic nickel coating was varied between the different simulations to study its effect on particle self-assembly. The end results of these simulations can be seen in Figs. 7 and 8. As can be seen in the figures, the magnetic dipole-directed assembly is very sensitive to variations in the strength of the magnetic interactions which are caused by changing the thickness of the nickel layer. Initially, nanorods are randomly distributed and oriented in the square as shown in Fig. 7a. The particles are below the superparamagnetic limit due to a lack of magnetic material, as evident from the disordered magnetic dipole moments. No assembly was observed for nickel thicknesses below 2 nm (results not shown) as the particles never exceed the superparamagnetic limit. However, particle interaction became noticeable for a 2-nm nickel layer, as evident from Fig. 7b which shows some particles assembling into short chains. For a nickel coating of 5 nm, the assembly is much more pronounced. Figure 8a shows the tendency of the particles to align head-to-tail with the particles forming multiple long chains. Increasing the amount of magnetic material even further leads to the formation of open ring-like structures (Fig. 8b) and even longer chains that attach to one another to form a network (Fig. 8c). Figure 8d shows particles with a nickel coating of 20-nm thickness. Three distinct ring shapes can be distinguished: one incorporated into a single chain and two consisting of two chains in close contact with each other. This configuration suggests that rings are formed by the merging of multiple chains, rather than the bending of a single chain. This is consistent with the observations Wen et al. (1999) made when simulating the ring formation of spherical particles. It is interesting to note that these rings do not adopt the "flux-closure" configuration, but a configuration more akin to what is referred to as the "onion" state in literature (Rothman et al. 2001). These rings are best described as a bifurcation of a single chain into two different paths, which eventually come together at a single point.

The strengthening of dipolar interactions with increasing nickel concentrations agrees well with experimental results. Analogous to the particles seen in the experiments, the modeled particles form rings and chains that combine into a network when the magnetic interactions are sufficiently strong. Weaker interactions lead to the formation of short chains and small particle clusters. When compared to the experimental results, the modeled rings in Fig. 8 have a significantly higher amount of nanorods in them. This also leads to larger ring diameters.

Previous research shows strong evidence that the formation of nanorings takes place in solution during the coating procedure rather than during the drying process (Ahmed et al. 2010). As such, owing to its 2D nature, the simulation model is unable to completely reproduce the experimental conditions and results. Stacks of rings, such as the ones that can be seen in Fig. 2c, d, are likely formed during the drying process, as individual rings are deposited atop one another due to the decreasing liquid volume. Owing to the lack of the third dimension, these structures cannot be reproduced by the simulation model. In addition, the absence of the third dimension reduces the mobility of the nanoparticles, effectively increasing their concentration. Varying the fractional area coverage ξ shows that the concentration of the nanoparticles plays an important role in their assembly into superstructures, as can be seen in Fig. 9. For increasing values of ξ, the tendency of the nanorods to bend into rings also increases. For low values of ξ, misaligned rods or chains of rods can reduce their magnetic energy by increasing the distance between one another, potentially leading to the formation of separate clusters such as those seen in Fig. 8. For higher values of ξ, the rods are constrained to a smaller area which makes it impossible for them to sufficiently increase their mutual distance. In this case, ring formation is the only effective way in which the system energy can be

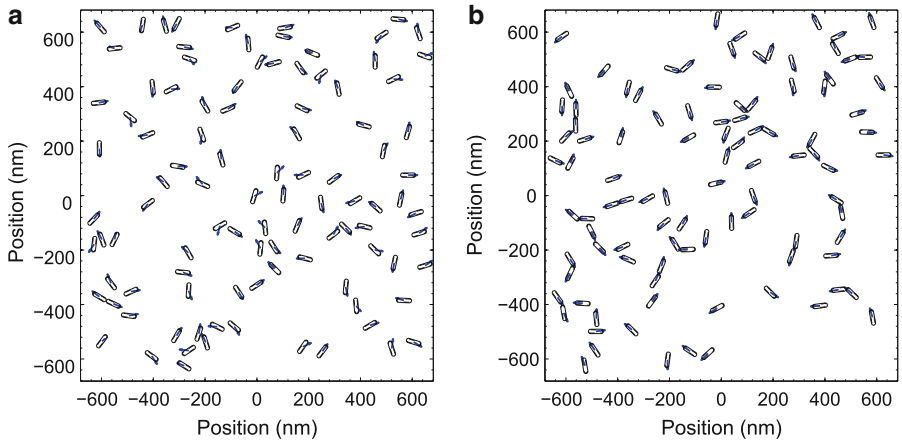

Fig. 7 Nanoparticles with a core aspect ratio of 4.5, a short core diameter of 12 nm, and a nickel layer thickness of 2 nm. The fractional area coverage ξ is equal to 0.05 and $\lambda = 0.67$. The *arrows indicate* the direction of the magnetisation vector. **a** Initial random orientation of nanoparticles at the beginning of the simulation. **b** The same system of nanoparticles after reaching a minimum free energy state. (colour online)

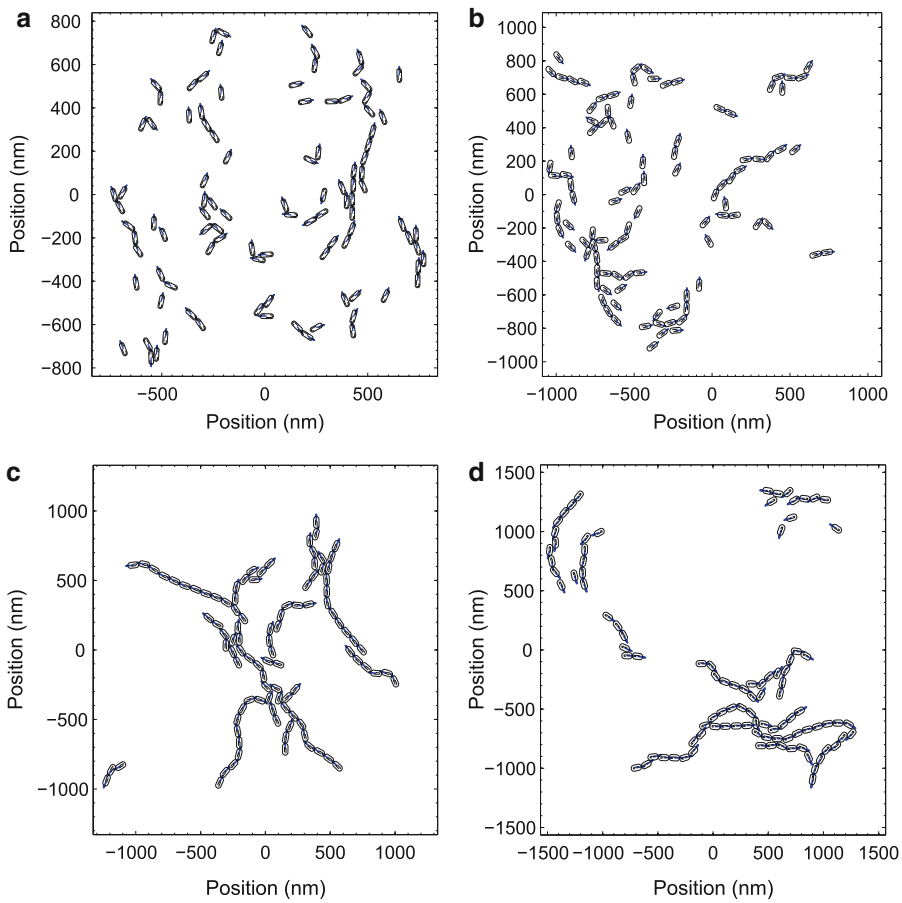

Fig. 8 Minimum free energy end states calculated for particles with a nickel coating of **a** 5 nm ($\lambda = 5.2$), **b** 10 nm ($\lambda = 27$), **c** 15 nm ($\lambda = 76$), and **d** 20 nm ($\lambda = 160$) thickness. All nanoparticles have a core aspect ratio of 4.5 and a short core diameter of 12 nm. The fractional area coverage ξ is equal to 0.05. The *arrows indicate* the direction of the magnetisation vector. (colour online)

lowered. This leads to single clusters of nanorings, similar to those observed in the experimental results. Higher values of ξ also lower the minimum coating thickness threshold for which ring formation is observed. For $\xi \geq 0.10$, the nanoparticles assemble into rings for a nickel coating of only 5 nm, whereas

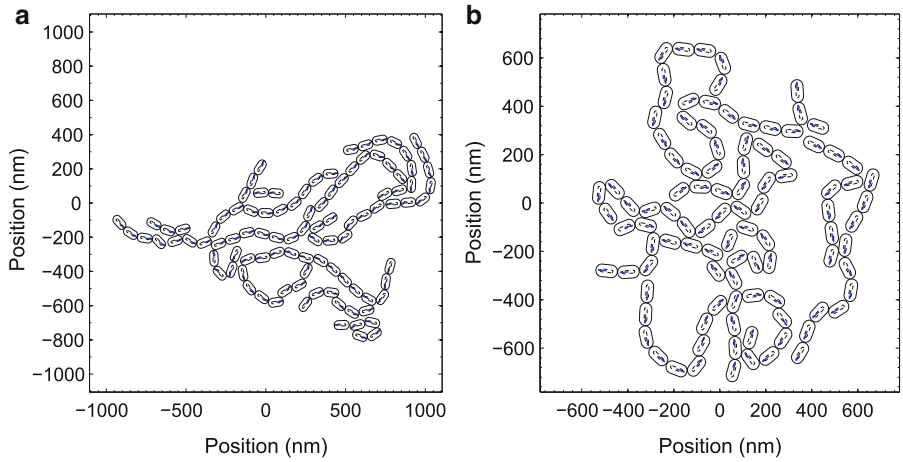

Fig. 9 Minimum free energy end states calculated for particles with a nickel coating of 20 nm ($\lambda = 160$) thickness. The fractional area coverage ξ is equal to 0.10 (**a**) and 0.20 (**b**). All nanoparticles have a core aspect ratio of 4.5 and a short core diameter of 12 nm. The *arrows indicate* the direction of the magnetisation vector. (colour online)

for $\xi \geq 0.25$ even a nickel coating of 2 nm is sufficient for the formation of superstructures. Increasing ξ also tends to lower the amount of nanorods per ring and, as a result, the average diameter of each ring.

Because ring formation takes place during the coating process, it is difficult to determine the "right" value for ξ. While the concentration of nanorods is quite low during the platinum-assisted coating method, the increasing magnetic interactions between them will eventually lead to a large local concentration of nanorods before ring formation.

Conclusions

The dipole-directed ring assembly of nickel-coated gold nanorods through the use of two distinct methods has been presented. The formation of nanochains has been observed for both coating methods when using relatively small amounts of nickel during synthesis. Increasing the nickel concentration in the growth solution leads to the formation of nanorings when using the platinum-assisted growth method and nanowires when using the fast growth method. The different results for both coating methods show the sensitivity of nanorod self-assembly to the rate at which the coating takes place, which is influenced by factors such as reaction temperature and reagent concentrations. The presence or absence of a surfactant during the nickel coating procedure also plays a role in determining the final assembly. The transition from nanochains to nanorings and -wires for increasing nickel concentrations show that the thickness of the nickel coating has a profound influence on the dipole directed assembly. 2D Monte Carlo simulations confirmed the tendency of the coated particles to assemble into nanochains and nanorings for different coating thicknesses, without the need to explicitly treat steric and van der Waals forces.

Acknowledgements The authors would like to thank Gregor Hlawacek for operating the helium ion microscope. One of the authors (WA) acknowledges support from the Higher Education Commission in Pakistan.

References

Ahmed W, Laarman RPB, Hellenthal C, Kooij ES, Van Silfhout A, Poelsema B (2010) Dipole directed ring assembly of Ni-coated Au-nanorods. Chem Commun 46:6711–6713

Aoshima M, Satoh A (2006) Two-dimensional Monte Carlo simulations of a colloidal dispersion composed of rod-like ferromagnetic particles in the absence of an applied magnetic field. J Colloid Interface Sci 293:77–87

Butter K, Bomans PHH, Fredrik PM, Vroege GJ, Philipse AP (2003) Direct observation of dipolar chains in iron ferrofluids by cryogenic electron microscopy. Nature Mater 2:88–91

Chen DH, Hsieh CH (2002) Synthesis of nickel nanoparticles in aqueous cationic surfactant solutions. J Mater Chem 12: 2412–2415

Gao J, Bender CM, Murphy CJ (2003) Dependence of the gold nanorod aspect ratio on the nature of the directing surfactant in aqueous solution. Langmuir 19:9065–9070

Griffiths DJ (1999) Introduction to electrodynamics. Prentice-Hall International, Upper Saddle River

Grzelczak M, Rodríguez-González B, Pérez-Juste J, Liz-Marzán LM (2007) Quasi-epitaxial growth of Ni nanoshells on Au nanorods. Adv Mater 19:2262–2266

Hyeon T (2003) Chemical synthesis of magnetic nanoparticles. Chem Commun 9:927–934

Johnson CJ, Dujardin E, Davis SA, Murphy CJ, Mann S (2002) Growth and form of gold nanorods prepared by seed-mediated, surfactant-directed synthesis. J Mater Chem 12: 1765–1770

Kodama RH, Berkowitz AE (1999) Atomic-scale magnetic modeling of oxide nanoparticles. Phys Rev B 59: 6321–6336

Kooij ES, Poelsema B (2006) Shape and size effects in the optical properties of metallic nanorods. Phys Chem Chem Phys 8:3349–3357

Liu CM, Guo L, Wang RM, Deng Y, Xu HB, Yang S (2004) Magnetic nanochains of metal formed by assembly of small nanoparticles. Chem Commun 23:2726–2727

Liu M, Guyot-Sionnest P (2005) Mechanism of silver(I)-assisted growth of gold nanorods and bipyramids. J Phys Chem B 109:22,192–22,200

Min Y, Akbulut M, Kristiansen K, Golan Y, Israelachvili J (2008) The role of interparticle and external forces in nanoparticle assembly. Nature Mater 7:527–538

Morimoto H, Katano K, Maekawa T (2009) Ring-chain structural transitions in a ferromagnetic particles system induced by a dc magnetic field. J Chem Phys 131:034,905–1–034,905–5

Nikoobakht B, El-Sayed MA (2003) Preparation and growth mechanism of gold nanorods (NRs) using seed-mediated growth method. Chem Mater 15:1957–1962

Orendorff CJ, Murphy CJ (2006) Quantitation of metal content in the silver-assisted growth of gold nanorods. J Phys Chem B 110:3990–3994

Pacholski C, Kornowski A, Weller H (2002) Self-assembly of ZnO: from nanodots to nanorods. Angew Chem Int Ed 41:1188–1191

Rothman J, Klui M, Lopez-Diaz L, Vaz CAF, Bleloch A, Bland JAC, Cui Z, Speaks R (2001) Observation of a bi-domain state and nucleation free switching in mesoscopic ring magnets. Phys Rev Lett 86:1098–1101

Sajanlal PR, Pradeep T (2010) Magnetic mesoflowers: synthesis, assembly, and magnetic properties. J Phys Chem C 114:16,051–16,059

Satoh A (1992) A new technique for metropolis Monte Carlo simulation to capture aggregate structures of fine particles: cluster-moving Monte Carlo algorithm. J Colloid Interface Sci 150:461–472

Satoh A (2008) Three-dimensional monte carlo simulations of internal aggregate structures in a colloidal dispersion composed of rod-like particles with magnetic moment normal to the particle axis. J Colloid Interface Sci 318: 68–81

Schmid G (2004) Nanoparticles: from theory to application. Wiley-VCH, Weinheim

Shevchenko EV, Talapin DV, Schnablegger H, Kornowski A, Festin O, Svedlindh P, Haase M, Weller H (2003) Study of nucleation and growth in the organometallic synthesis of magnetic alloy nanocrystals: the role of nucleation rate in size control of $CoPt_3$ nanocrystals. J Am Chem Soc 125: 9090–9101

Shine AD, Armstrong RC (1987) The rotation of a suspended axisymmetric ellipsoid in a magnetic field. Rheol Acta 26:152–161

Sobal NS, Hilgendorff M, Möhwald H, Giersig M, Spasova M, Radetic T, Farle M (2002) Synthesis and structure of colloidal bimetallic nanocrystals: the non-alloying system Ag/Co. Nano Lett 2:621–624

Sun S, Anders S, Thomson T, Baglin JEE, Toney MF, Hamann HF, Murray CB, Terris BD (2003) Controlled synthesis and assembly of FePt nanoparticles. J Phys Chem B 107:5419 – 5425

Tavares JM, Weis JJ, Telo da Gama MM (2002) Quasi-two-dimensional dipolar fluid at low densities: Monte Carlo simulations and theory. Phys Rev E 65:061201–0612011

Tripp SL, Pusztay SV, Ribbe AE, Wei A (2002) Self-assembly of cobalt nanoparticle rings. J Am Chem Soc 124:7914–7915

Vereda F, De Vicente J, Hidalgo-Álvarez R (2009) Physical properties of elongated magnetic particles: magnetization and friction coefficient anisotropics. ChemPhysChem 10: 1165–1179

Wang H, Chen QW, Sun LX, Qi HP, Yang X, Zhou S, Xiong J (2009) Magnetic-field-induced formation of one-dimensional magnetite nanochains. Langmuir 25:7135–7139

Wang N, Cao X, Kong D, Chen W, Guo L, Chen C (2008) Nickel chains assembled by hollow microspheres and their magnetic properties. J Phys Chem C 112:6613–6619

Wei A, Tripp SL, Liu J, Kasama T, Dunin-Borkowski RE (2009) Calixarene-stabilised cobalt nanoparticle rings: self-assembly and collective magnetic properties. Sup Chem 21: 189–195

Wen W, Kun F, Pál KF, Zheng DW, Tu KN (1999) Aggregation kinetics and stability of structures formed by magnetic microspheres. Phys Rev E 59:R4758–R4761

Wu SH, Chen DH (2004) Synthesis and stabilization of Ni nanoparticles in a pure aqueous CTAB solution. Chem Lett 33:406–407

Xiong Y, Ye J, Gu X, Chen QW (2007) Synthesis and assembly of magnetite nanocubes into flux-closure rings. J Phys Chem C 111:6998–7003

Zhang X, Zhang Z, Glotzer SC (2007) Simulation study of dipole-induced self-assembly of nanocubes. J Phys Chem C 111:4132–4137

Zitoun D, Respaud M, Fromen MC, Casanove MJ, Lecante P, Amiens C, Chaudret B (2002) Magnetic enhancement in nanoscale CoRh particles. Phys Rev Lett 89:372,031–372, 034